Planar 200-GHz Transceiver Modules

Amirreza Alizadeh, *Member, IEEE*, Utku Soylu, *Student Member, IEEE*, Logan Whitaker, Biljana Stamenic, Demis D. John, Munkyu Seo, *Senior Member, IEEE*, Ahmed S. H. Ahmed, and Mark J. W. Rodwell, *Fellow, IEEE*

***Abstract*—We report planar 200-GHz transmitter and receiver modules for high-frequency, high-capacity wireless transmission. The modues were used for 8-Gbaud 16QAM data transmission (32 Gb/s) over 7.1 m, featuring 13.4% RMS EVM on a link with 10.4 dB added attenuation. The modules are compact and highly integrated, with only a passive antenna substrate and a single transmitter or receiver integrated circuit (IC) providing the transmitter and receiver radio-frequency (RF) front-end functions, avoiding the size and cost of machined waveguide interfaces. The transmitter module contains a single indium phosphide (InP) IC, with (*I*,*Q*) baseband inputs, frequency upconversion, and a power amplifier (PA), and it is wire-bonded using a wedge-bonder to a passive fused silica antenna substrate that carries a 2×2 patch antenna array and an impedance-matching network that matches the transmitter IC to the combined impedances of the antenna array and the IC-antenna wire-bond. The antenna radiation pattern has a beamwidth designed to couple efficiently to external polytetrafluoroethylene (PTFE) lenses having a 0.56 numerical aperture. The receiver module is similar. The transmitter module has a measured ±25° beamwidth in the *E*-plane and *H*-plane, a measured peak equivalent isotropic radiated power (EIRP) of 24 dBm, with the EIRP remaining greater than 19 dBm over 200-218 GHz. The receiver module has 29.4 dB peak conversion gain with 3-dB bandwidth of 14 GHz (from 194 to 208 GHz).**

***Index Terms*—Antenna, heterojunction bipolar transistor (HBT), glass, indium phosphide (InP), mm-wave, patch antenna, quartz, receiver, transmitter.**

I. Introduction

THE 100-300 GHz frequency range has potential application in high-capacity, short-range backhaul data transmission links. The wide available bandwidths can support high modulation symbol rates, and hence high per-channel data rates. Additionally, because the wavelengths are short, even compact line-of-sight multiple-input multiple-output (MIMO) arrays can support many simultaneous independent signal beams, further increasing the transmission capacity [1]–[4].

These links require RF front-end modules interfacing the transmitter and receiver integrated circuits to high-frequency antennas. There has been extensive development of *D*-band (110-170 GHz) transceiver modules [5], including designs using simple ball-bonded wirebonds to printed-circuit-board (PCB) antennas [6]–[8], membrane interfaces to waveguide [9], and ICs flip-chip bonded to interposers carrying antennas [10]–[15]. Printed circuit boards and interposers can be fabricated from low-ϵ_r materials, which permits the design of antennas having high radiation efficiency.

The higher frequency 140-220 GHz (*G*-band) and 220-330 GHz (*WR*-3 waveguide) bands offer further increase in bandwidth and further reductions in required MIMO array lengths [16], [17]. In the modules reported in [18]–[26], the transceiver ICs are directly interfaced to the waveguide through wire bonds. 100-300 GHz waveguide interfaces require precisely controlled dimensions, hence these are expensive to machine, particularly if the transmitter and receiver are each assembled from multiple ICs, each packaged in a separate waveguide module.

An alternative is to use antennas fabricated on the transceiver ICs themselves (i.e., antenna-on-chip), including designs reported in *D*-band [27], [28], at 240 GHz [29], and at 300 GHz [30]. The high dielectric constants (ϵ_r) of III-V and silicon semiconductor substrates can result in most of the antenna radiated power coupling into dielectric slab modes of the IC substrate, with consequently low antenna radiation efficiency. Refractive-index-matched hemispherical or hyper-hemispherical lenses placed on the IC back substrate [31] can improve the efficiency of on-chip antennas. Furthermore, an antenna array on the chip having ±25° beamwidth would consume $\approx \lambda_0^2/2$ die area ($\approx 1.0\,\mathrm{mm}^2$ at 200 GHz), significantly increasing the cost of the system.

Here, we report 210-GHz transmitter and receiver modules using planar packaging to avoid waveguide interfaces and their associated machining costs (Fig. 1). In these modules, the InP heterojunction bipolar transistor (HBT) [32] direct-conversion transmitter and receiver ICs are connected, by wire bonds, to 2×2 microstrip patch antenna arrays on fused silica (FS) substrates. Shown in Fig. 1(c), the antenna arrays are designed to be coupled to external PTFE lenses that have 50 mm diameter and 37.5 mm focal length ($NA = 0.56$), featuring 40.4 dB aperture directivity if uniformly illuminated. For efficient coupling, the 3-dB beamwidth of the antenna array (θ_{ant}) is designed to be less than the lens acceptance angle $\theta_{\text{lens}} = 2\arctan(25\,\mathrm{mm}/37.5\,\mathrm{mm}) = 68^\circ$. The 50-$\mu$m antenna

Manuscript received August 22, 2023; revised March 20, 2024. This work was supported in part by the Semiconductor Research Corporation and in part by the Defense Advanced Research Projects Agency (DARPA) through the Joint University Microelectronics Program (JUMP). This work was also partially supported by the Institute of Information & Communications Technology Planning & Evaluation (IITP) Grant 2021-0-00198 (Development of key technologies for 6G RF front-end based on low-power MIMO and highly efficient spatial QAM synthesis) funded by the Korean Government (MSIT).

A. Alizadeh was with the Department of Electrical and Computer Engineering, University of California at Santa Barbara, Santa Barbara, CA 93117 USA. He is now with Keysight Technologies, Santa Rosa, CA 95403 USA. (e-mail: aliz@ucsb.edu).

U. Soylu was with the Department of Electrical and Computer Engineering, University of California at Santa Barbara, Santa Barbara, CA 93117 USA. He is now with IBM Research Center, Yorktown, NY 10598 USA.

M. Seo is with the Department of Electrical and Computer Engineering, Sungkyunkwan University, Suwon 440-746, South Korea.

A. S. H. Ahmed is with Analog Devices Inc., Cairo 11835, Egypt.

L. Whitaker, B. Stamenic, D. D. John, and M. J. W. Rodwell are with the Department of Electrical and Computer Engineering, University of California at Santa Barbara, Santa Barbara, CA 93117 USA.

This space is intentionally left blank for further information.

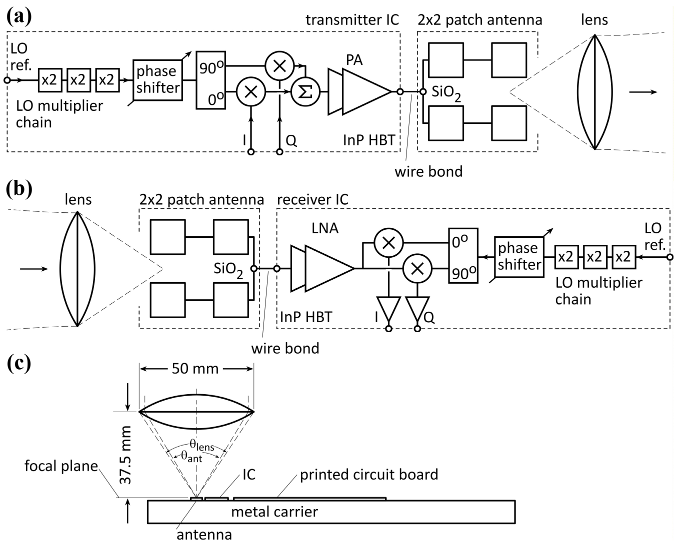

Fig. 1. Block diagrams for the (a) transmitter and (b) receiver modules. The InP HBT transmitter and receiver ICs are wire-bonded to 2×2 patch antenna arrays on fused silica substrates. (c) The 2×2 patch antenna arrays are coupled to external PTFE focusing lenses with 37.5 mm focal length and 50 mm diameter.

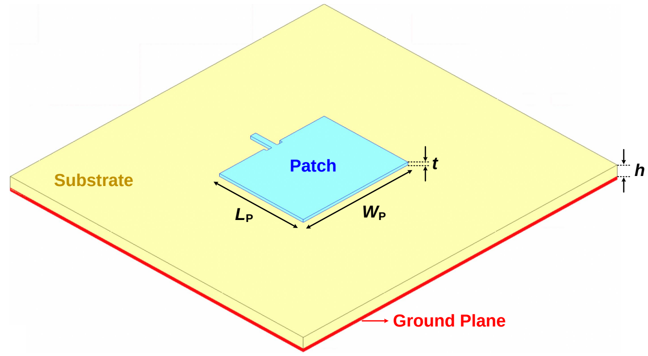

Fig. 2. Microstrip patch antenna on fused-silica substrate. Design parameters are $\epsilon_r \approx 3.8$, $h = 50\,\mu$m, and $t = 0.2\,\mu$m.

substrate and the low dielectric constant (i.e., $\epsilon_r = 3.8$) both reduce the coupling of the antenna radiation into dielectric slab modes.

This paper addresses antenna design (Section II) and fabrication (Section III), three-dimensional (3D) electromagnetic design and modeling of the IC-antenna interface (Section V), and transmitter and receiver performance measurements (Section VI). The design and performance of the InP ICs have been previously reported [33]–[35], and therefore, here we only briefly review their performance to use their data for designing the IC-antenna interface and as a reference for module results (Section IV). Data transmission experiments using these modules have been reported in [36], which is briefly discussed in (Section VI-C). This paper is concluded in Section VII.

II. 50-Ω-Matched 2×2 Patch Antenna Array

Microstrip patch antennas are planar, compatible with monolithic microwave integrated circuit (MMIC) technology, and inexpensive to fabricate [37], [38]. However, their relatively low efficiency, spurious feed line radiation, and very narrow frequency bandwidth (a few percent) are challenges at mm-wave frequencies [38], [39]. Fig. 2 shows a 210-GHz patch antenna realized on a 50-μm-thick FS substrate with $\epsilon_r \approx 3.8$. The metal is a 200-nm thick Au layer with a 4-nm thick Cr adhesion layer between the Au and the FS substrate. There are four main considerations for the design of patch antennas [38]:

1) The metal (patch) thickness should be very small compared to the free-space wavelength ($t \ll \lambda_0$).
2) Substrate thickness (h) should be a very small fraction of λ_0, often $0.003\lambda_0 \leq h \leq 0.05\lambda_0$.
3) The patch length (L_P) is approximately half of the wavelength in the dielectric ($\lambda_d = \lambda_0/\epsilon_r^{0.5}$).
4) The patch width (W_P) can be estimated as

$$W_P \approx \frac{c}{2f_0}\sqrt{\frac{2}{\epsilon_r + 1}}, \tag{1}$$

where c is the free-space speed of light, and f_0 is the antenna resonant frequency.

For an FS substrate with $\epsilon_r = 3.8$ at 210 GHz, we have $\lambda_0 = 1.43$ mm and $\lambda_d = 0.73$ mm. This leads to $W_P \approx 0.46$ mm and $L_P \approx 0.34$ mm. Furthermore, the substrate thickness should be between $4.3\,\mu$m and $71.5\,\mu$m. Thick substrates with low dielectric constant often provide greater antenna efficiency and bandwidth [38], [39]. Nonetheless, the main challenge of using thick substrates is strong coupling of microstrip lines to surface wave modes, which results in strong feed line radiation (Section II-B), which can then degrade the antenna radiation pattern and efficiency. In this work, we used an FS substrate with $50\,\mu$m thickness, as this was the thinnest commercially available substrate, thinner substrates being extremely fragile.

A. Slotted Patch Antenna

The fractional bandwidth of a simple rectangular patch antenna (Fig. 2) is low [37]–[39], potentially limiting the overall bandwidth of the receiver and transmitter modules. At RF and microwave frequencies, patch antennas on multilayer PCBs have achieved over 35% fractional bandwidth by employing wideband techniques such as aperture coupling and differential L-probe feeding [40]–[42]. Slotted patch antennas have also demonstrated wider bandwidths than simple rectangular patch antennas [43]–[45]. Considering the high cost and logistics of building antennas on multilayer PCBs, we report a similar design to [43]–[45] here, but at a much higher frequency (210 GHz), and with a relatively thick substrate ($h = 0.068\lambda_d$).

Fig. 3 shows the design of the 210-GHz slotted patch antenna. Two slots, located at L_1 and L_2 from the symmetry line of the patch, are introduced in the structure to increase the bandwidth. D_1 and D_2 represent the depths of the first and second slots, respectively. Each slot creates an additional resonance in the input impedance (Z_{in}), and with appropriate design can extend the frequency range over which the input reflection coefficient (S_{11}) is better than -10 dB. Fig. 4 presents the simulated performance of a slotted patch antenna, with dimensions shown in Fig. 3, and of a simple rectangular patch

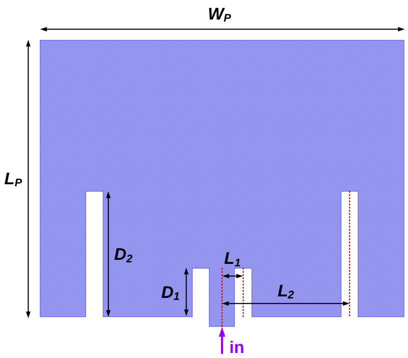

Fig. 3. 210-GHz slotted patch antenna on a 50-μm fused-silica substrate. Design parameters are $W_{\text{P}} = 428\,\mu$m, $L_{\text{P}} = 342\,\mu$m, $L_1 = 25\,\mu$m, $L_2 = 150\,\mu$m, $D_1 = 60\,\mu$m, and $D_2 = 155\,\mu$m.

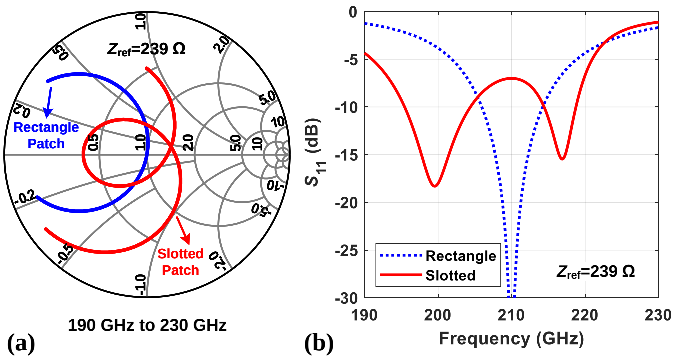

Fig. 4. Comparison between the simulated (a) input impedance (Z_{in}) and (b) S_{11} of a rectangular patch antenna (with $W_{\text{P}} = 400\,\mu$m and $L_{\text{P}} = 320\,\mu$m) versus its slotted counterpart shown in Fig. 3. Reference impedance is 239-Ω, which is the input impedance of the rectangular patch antenna at 210 GHz.

antenna, with $W_{\text{P}} = 400\,\mu$m and $L_{\text{P}} = 320\,\mu$m. Both antennas have a 210 GHz center frequency, and the optimal dimensions for both antennas were selected by extensive automatic layout optimization in Keysight ADS. The rectangular patch antenna has an input impedance of about 239 Ω at 210 GHz. Assuming a 239-Ω reference impedance, Fig. 4 shows that the slotted antenna has a wideband S_{11} response, and given that purely resistive impedances can be transformed over broad bandwidths, the slotted antenna can be matched over a bandwidth comparable to that, over which it shows a good reflection coefficient given a 239-Ω impedance normalization.

B. Feed-Line Radiation

In patch antennas (Fig. 2), a greater vertical separation between the antenna and the ground plane (h) results in greater antenna fractional bandwidth [38]. Unfortunately, for antenna feed network and the microstrip feed lines between antenna elements in a patch array, a greater h also results in higher coupling to the substrate dielectric slab modes [38], [39], [43]. This results in both greater feed network losses and greater parasitic feed line radiation, the latter degrading the array radiation pattern [38], [39], [43]. In patch antenna arrays implemented in multi-layer interposers and PCBs, the ground plane under microstrip feed lines can be placed only a small vertical separation away from the microstrip signal conductor, for small feed network losses, while the ground plane under the patch antenna can be placed at a larger vertical separation, for large antenna bandwidth [43]. This design strategy is, unfortunately, not feasible for an antenna array design using single plane of dielectric.

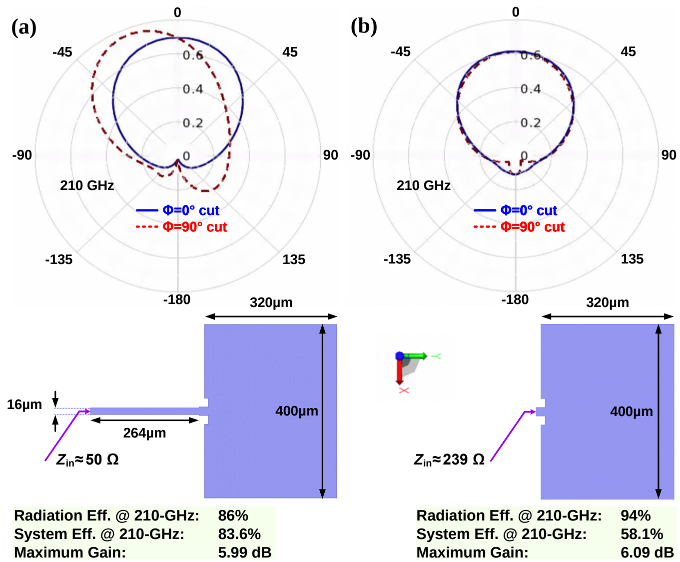

Fig. 5. Radiation patterns, antenna characteristic, and layouts of (a) 50-Ω-matched and (b) unmatched patch antennas on a 50-μm-thick fused-silica substrate. Matching to 50-Ω using the series microstrip line reduces the radiation efficiency from 94% to 86%, and radiation from the series line distorts the radiation pattern.

For the antenna arrays used in this work, the fabrication process offers only limited features, with only a single plane of dielectric having a ground plane below and one layer of patterned conductor above. Through-substrate vias are not available, nor are thin-film resistors or metal-insulator-metal capacitors. Impedance matching networks on the antenna substrate can therefore only use series microstrip lines and shunt open-circuit stubs. The large vertical distance between the microstrip signal line and the ground plane (i.e., $h = 50\,\mu\text{m} = 0.068\lambda_{\text{d}}$) results in significant coupling to the substrate dielectric slab modes, with associated feed-line radiation, particularly if transmission lines are wide. Wide microstrip lines ($W_{\text{TL}} \geq 30\,\mu$m) have particularly high radiation, and should be be avoided if possible. This narrows the choice of matching elements to high-Z_0 transmission-lines and open stubs, seriously constraining the design.

To illustrate the effect of feed-line radiation, even for narrow lines, Fig. 5 compares the performances of 210-GHz patch antennas, on a 50-μm thick FS substrate, with and without series-line impedance-matching networks. The matched antenna employs a $\lambda_{\text{g}}/4$ series line section (with 264 μm length and 16 μm width) for impedance matching to 50 Ω. Feed-line radiation tilts the H-plane pattern of the matched antenna (Fig. 5(a)), and therefore the radiation efficiency of the matched antenna (86%) is lower than that of its unmatched counterpart (94%).

Consequently, to minimize the beam tilt, maximize the radiation efficiency, and minimize the reflection coefficient, the feed network and patch antenna array were co-designed

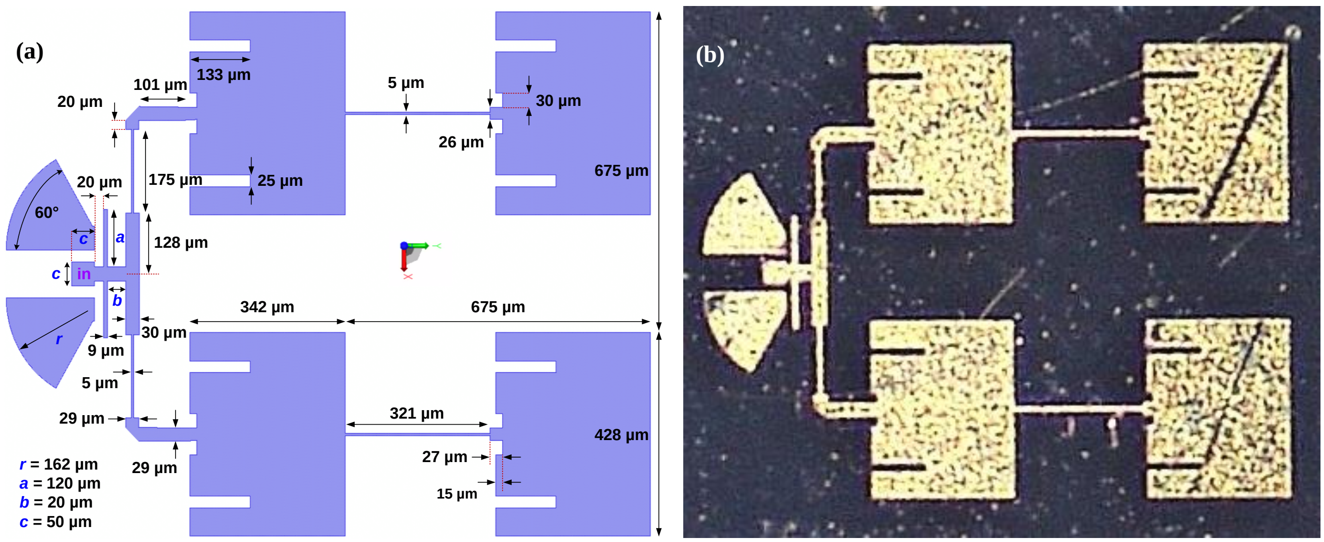

Fig. 6. (a) Layout and (b) photograph of the 50-Ω-matched corporate-fed 2×2 series patch-antenna array on a 50-μm thick fused-silica substrate. This array, a test structure, is contacted at the left with a ground-signal-ground (GSG) mm-wave wafer probe; $\lambda_d/4$ microstrip open-circuit radial stubs provide a low impedance to ground at the substrate top surface for the wafer probe ground pins.

and optimized using the FEM engine in Keysight RFpro.

C. 2×2 Series Patch Antenna Array

The transmitter and receiver patch antenna arrays were designed to couple to external PTFE lenses having 50 mm diameter and 37.5 mm focal length. The associated numerical aperture is $NA = \sin(\theta) = 0.55$, where $\theta = 34°$ is the maximum half-angle of the cone of radiation that can pass through the lens. The 2×2 array (Fig. 6) was therefore designed for 3-dB beam-widths smaller than ±34° in both E-plane and H-plane. If uniformly illuminated, the associated lens aperture directivity would be 40.8 dB. Nevertheless, the realized aperture directivity will be smaller than this because the antenna radiation into the lens is not uniform over the lens cross-section.

Three versions of the 2×2 antenna array were designed and fabricated. The first of these (Fig. 6) was designed to allow measurements of antenna gain, reflection coefficient, and beam pattern. The array has an input network providing a 2:1 power split between the two rows of antennas, while matching the input impedance to 50 Ω. The antennas in the second column are connected in series with those in the first column, and the spacing between the antennas in both directions is approximately $\lambda_0/2$ at 210 GHz. This test array interfaces to a 50 Ω system through mm-wave wafer probes. Consequently, given the absence of through-substrate-vias, $\lambda_d/4$ microstrip open-circuit radial stubs provide a low impedance to ground at the substrate top surface for the wafer probe ground pins. Similar antenna arrays were subsequently designed and fabricated for the transmitter and receiver modules.

Fig. 7(a) shows the gain and return loss of the 50-Ω-matched corporate-fed 2×2 patch-antenna array versus the frequency. While the measured S_{11} is better than −10 dB over more than 40-GHz bandwidth, the 3-dB (gain) bandwidth is about 20 GHz (192–212 GHz), with peak gain of 8.1 dB at 200 GHz. The measured peak gain (at 200 GHz) is 2 dB less than the

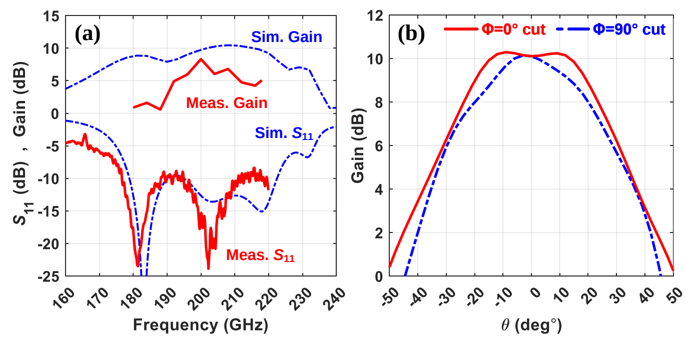

Fig. 7. 50-Ω-matched 2×2 patch-antenna array results: a) simulated and measured gain and S_{11} vs. frequency, and (b) simulated gain versus θ for $\phi = 0°$ and 90° cuts. 0° cut refers to the X-axis defined in Fig. 6 (the H-plane), whereas 90° cut refers to the Y-axis (the E-plane).

simulated peak gain at 210 GHz. The discrepancy could be a result of fabrication tolerances, EM-simulation inaccuracies, or measurement inaccuracies. Fig. 7(b) shows the simulated radiation pattern at 210-GHz, as a function of angle θ, for the E-plane and H-plane cuts. Measured radiation patterns will be shown subsequently for the transmitter and receiver modules.

III. Patch Antenna Array Fabrication

We briefly describe the antenna fabrication process so that the results can be reproduced. Antennas were fabricated on 50-μm thick fused-silica substrates. The 1 cm by 1 cm substrates, too fragile to clip directly onto an evaporator platen, were taped to a carrier substrate before depositing backside and frontside metallization (4-nm Cr/200-nm Au alloy) by E-beam evaporation. The substrates, too thin for the focal depth adjustment range of lithography systems available to us, were mounted to Si carriers prior to lithography. UV-6.08 photoresist was spun on the Si carrier as an adhesive, and the substrate was then placed onto the resist-covered carrier. After 1 minute at room temperature, the sample was baked at

100 degrees Celsius to wick away excess resist between the carrier and the substrate. The attachment resist had sufficiently uniform thickness for the optical lithography system to focus over the full area of the FS sample. The topside metal (antennas, feed network, matching network) was patterned by argon ion milling masked by photoresist (AZ5214 with an hexamethyldisilazane (HMDS) adhesion layer); a fluorine etch removed resist residue. The substrates were demounted from the Si carriers using N-methylpyrrolidone (NMP) followed by isopropyl alcohol (IPA)/ACE/IPA cleaning. To dice the 1 cm by 1 cm substrates into individual antenna arrays, the substrates were then remounted on Si carriers using Crystal Bond 509 clear adhesive. The antennas were then diced using 2187-4C-22RU-3 blades with a 53-mm flange. Chipping of the substrate edges during dicing made the dicing street width (the distance between the edge of substrate and the antenna bond pads) inconsistent, but this distance was approximately 100 $\pm$ 50 μm. Samples were then demounted using NMP followed by IPA/ACE/IPA.

IV. InP Receiver and Transmitter ICs

The InP transmitter and receiver ICs have been reported in detail in [33]–[35]. Below, we summarize the key IC design and performance features relevant to the design of the IC-antenna interface (Section V).

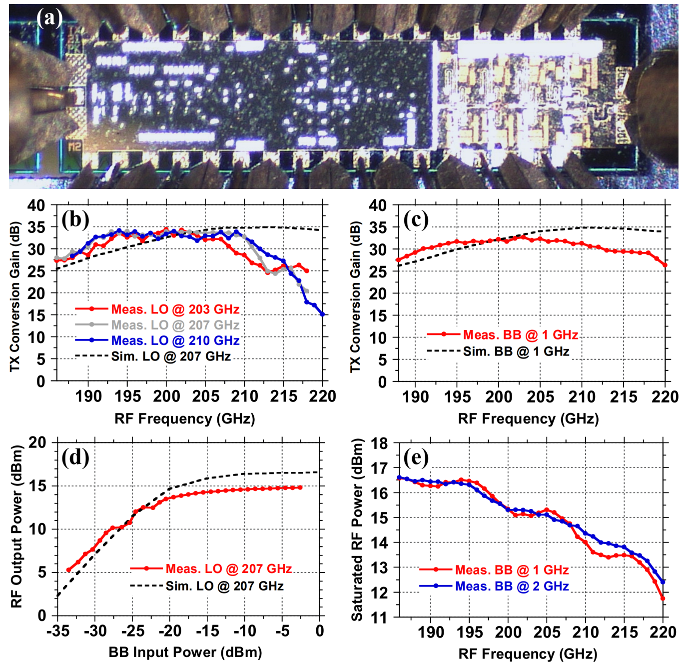

Fig. 8. 200-GHz transmitter IC: (a) chip photo, (b) conversion gain vs. output frequency at a fixed LO frequency, (c) conversion gain vs. output frequency for a fixed 1-GHz baseband input signal, (d) output power vs. baseband input power, and (e) saturated output power vs. RF frequency with a fixed 1- or 2-GHz baseband input signal and with the LO frequency varied.

A. 200-GHz InP Direct-Conversion Transmitter

The 200-GHz direct-conversion transmitter is presented in Figs. 1(a) and 8(a). It consists of an 8:1 local-oscillator (LO) frequency multiplier, a phase-shifter, a quadrature phase splitter, an *I*-*Q* upconversion mixer, a pre-driver, and a PA. The 8:1 frequency multiplier uses three cascaded push-push frequency doublers [33]. The phase-shifter employs an *I*-*Q* vector modulator in its core and is deployed in the LO path (as opposed to the RF path) to make the IC performance less sensitive to the bandwidth and linearity of the phase-shifter [33]. A Lange coupler splits the LO into two phases, and gain blocks in the LO and RF paths are realized using cascaded common-base (CB) amplifiers [33]. The up-conversion mixer consists of two double-balanced (Gilbert cell) mixers; the *I* and *Q* port bandwidths are about 20 GHz [33].

The PA employs four capacitively degenerated CB stages and in simulation provides 20 dB gain and 50 mW saturated output power (P_{sat}) at 200 GHz. The design is similar to [35], except that 2:1 less power-combining is used. As shown in Fig. 8(b-e), in measurements, the transmitter IC shows a peak conversion gain of 34 dB at 200 GHz, and the 3-dB bandwidth is about 20 GHz. The measured output power at 1-dB compression point ($P_{\text{out-1dB}}$) for $f_{\text{LO}} = 207$ GHz is approximately 11 dBm, and P_{sat} is 14–16.5 dBm over 190–210 GHz.

B. 200-GHz InP Direct-Conversion Receiver

Shown in Figs. 1(b) and 9(a), the receiver IC uses the same LO frequency multiplier chain as the transmitter. The low-noise amplifier (LNA) uses three cascade capacitively-degenerated CB stages [33], [34]. Similar to the transmitter mixer, the receiver *I*-*Q* mixer consists of two double-balanced cores and is followed by an emitter-degenerated differential pair to drive the external 50-Ω load [33]. In measurements, the receiver, when operated with a 207-GHz LO, shows 24 dB peak conversion gain at 197 GHz and approximately 20 GHz bandwidth (Fig. 9(b)). With a fixed 1-GHz baseband input, but with the LO frequency varied, the conversion gain is $>$ 20 dB over 190–206 GHz (Fig. 9(c)). At 206 GHz, the baseband input power at receiver 1-dB compression ($P_{\text{in-1dB}}$) is -22 dBm. The measured noise-figure is less than 8.5 dB over 200–211 GHz frequency range (Fig. 9(e)).

V. Design of the IC-Antenna Interface

The InP ICs were connected to the antennas using 20-μm diameter Au round bond-wires. Bonds were formed by wedge bonding, as opposed to ball bonding, since the feasible bond vertical looping is smaller with wedge bonding, providing a lower bond inductance [46]. Consistent with the findings of [46], given the constraint of ribbon width or round wire diameter, each smaller than the IC and antenna bond pad widths, in our electromagnetic simulations, wedge-bonded ribbon bonds did not show smaller inductive reactance than wedge-bonded round wires. As a result, round bond-wires were used in this work.

Because the ICs had already been designed and fabricated prior to designing the antenna arrays, the IC-antenna interface parasitics associated with the wire-bond must be compensated by the impedance matching network on the antenna substrate. In addition to the connections between the signal lines, the IC-antenna connection also requires a connection between

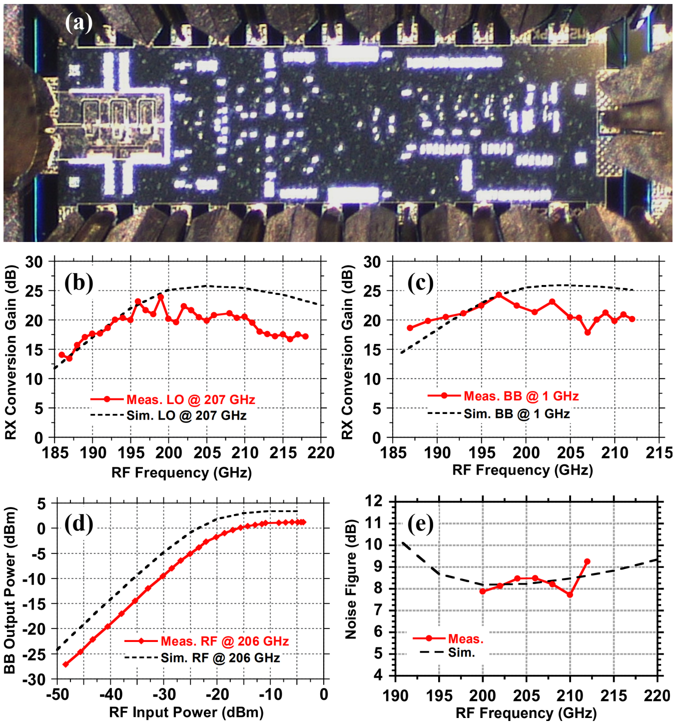

Fig. 9. 200-GHz RX IC: (a) chip photo, (b) conversion gain vs. input RF frequency for $f_{\mathrm{LO}} = 207\,\mathrm{GHz}$, (c) conversion gain vs. input RF frequency when f_{LO} is varied to achieve a down-converted signal at 1 GHz, (d) output power of the RX versus the RF input power at 206 GHz, and (e) noise figure.

the ground plane on the InP IC top surface and the antenna array substrate back surface. The ground-ground connection can be provided by through-substrate vias (TSVs) on the InP ICs or wire-bonding the ground pads on the InP IC to the ground pads on the antenna. This will be further discussed in Section V-A. Finally, the transmitter IC's PA and the receiver IC's LNA, both designed for best performance at 210 GHz, in measurements showed best performance at lower frequencies [33]–[35]. Thus, the impedance-matching networks on the transmitter and receiver antenna arrays were designed to shift the frequency of best performance of the PA and LNA towards 210 GHz.

A. Ground Transition

Fig. 10 shows a cross-section and an oblique view of the IC-antenna interface in the transmitter module. The InP IC and the antenna array were mounted, with their diced edges touching, onto an Au-Ni-plated Cu carrier. The die-attach adhesive is a conductive, Ag-filled epoxy. The antenna ground plane and the InP IC backside metal are thus connected and form a continuous conducting metal plane. On the InP IC, signals are carried on microstrip lines with Metal-4 (M4) as the microstrip signal conductor and Metal-1 (M1) as the local ground plane of the microstrip on the top surface of the IC. At the ground-signal-ground (GSG) IC bond pads, M1-M4 vias connect the ground bond pads, on M4, to the M1 ground plane below the pads. On the antenna substrate, the microstrip signal conductor is on the fused silica top surface, and the microstrip ground plane is on the fused silica bottom surface. Thus, connections

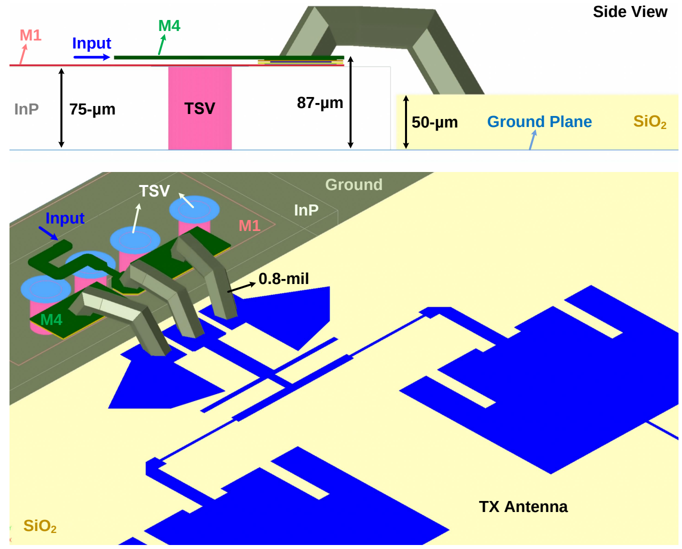

Fig. 10. IC-antenna interface in the transmitter module. The point labeled "Input" defines the reference plane for electromagnetic simulations of the IC-antenna interface.

must be provided between the IC and antenna signal lines and between the IC and antenna ground planes. The signal lines are connected with simple wedge-bonded wire bonds using 20-μm diameter Au wire.

As previously explained, the antenna ground plane and the InP IC backside metal are connected and form a continuous metal plane. TSVs in the InP IC connect the M1 ground plane to the InP IC backside metal, and if appropriately placed, can provide a connection, with low series impedance, between the M1 ground plane and the antenna ground plane. Unfortunately, because the IC-antenna transition was not simulated at the time of design of the transmitter IC, the TSVs on the InP transmitter IC were poorly located, and the resulting impedance between the M1 ground plane and the InP backside metal, through the InP TSVs, is high at 160-220 GHz. To address this issue, additional ground-ground connections between the transmitter IC and the antenna array substrate were provided by wire bonds. Demonstrated in Fig. 10, these wire-bonds, again wedge-bonded with 20-μm diameter Au wire, connect M4 ground pads on the InP IC to top-surface ground pads on the antenna substrate. Microstrip $\lambda_g/4$ radial stubs (at 210 GHz) connected to these bond pads provide a low impedance from the bond pads to the antenna substrate ground plane.

To elaborate on the impact of the ground bondwires on ground transition, we simulated a transition between a 50-Ω microstrip line on the InP IC, through a 20-μm diameter wire bond, to a 50-Ω microstrip line on the antenna substrate (Fig. 11). In this simulation, the TSVs are located in the same positions as in the fabricated InP transmitter IC. We simulated both the case with the supplementary top-surface ground-ground connections (Fig. 11(a)), and the case where the only antenna-IC ground connection is through the InP TSVs (Fig. 11(b)). Without supplementary ground-ground connections, at 200 GHz the insertion loss is approximately 3 dB, while the return loss is approximately 5 dB. Adding the supplementary ground-ground bonds significantly improves

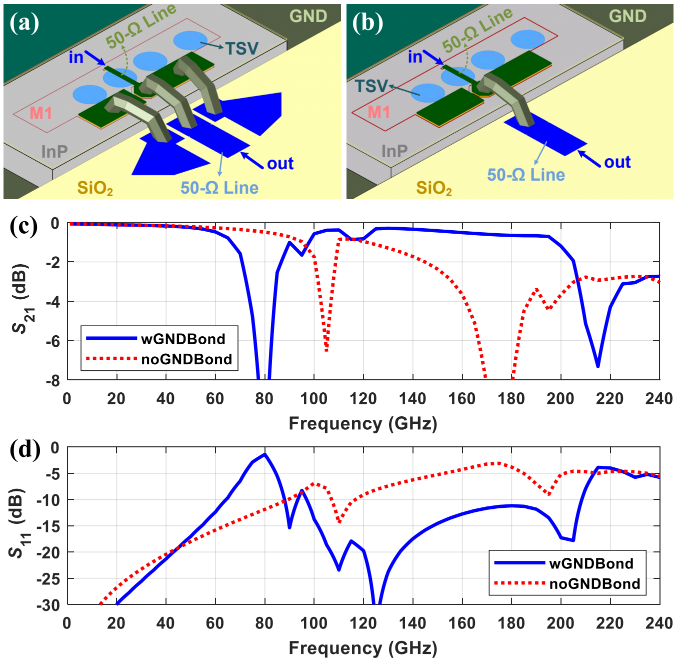

Fig. 11. Back-to-back connection of microstrip 50-Ω lines on the InP IC and on the fused-silica substrate (a) with and (b) without supplementary wire bonds between the IC and antenna ground pads. The simulated S_{21} and S_{11} of the transitions are shown in (c) and (d). The points labeled "In" define the reference planes for EM simulations of the IC-antenna interfaces. TSVs are located in the same positions as in the fabricated InP transmitter IC.

the performance, with only 1 dB simulated insertion loss and better than 15 dB return loss at 200-GHz.

Simulations of Fig. 11 were also repeated for the case where the TSVs were located in the same positions as in the fabricated InP receiver IC. The simulation results show that, unlike the transmitter IC, the TSVs in the receiver IC are more fortuitously placed, and the impedance at 200 GHz between the top-surface and back-surface ground planes is sufficiently low, such that the additional ground wire-bond connections between the receiver IC and the antenna substrate are not necessary.

B. Transmitter Interface

The InP transmitter IC, though designed for peak output power at 210 GHz, in measurements showed maximum P_{sat} at 185-190 GHz (Fig. 8(e)), lower than the desired frequency of operation of the transmitter module. The impedance matching network on the antenna substrate (Fig. 10) was therefore designed to shift the frequency of peak transmitter output power to 210 GHz. To design this matching network, we first simulated the transmitter P_{sat} over 190–230 GHz, at 1-GHz frequency increments, as a function of load impedance at each frequency, with the simulation reference plane as indicated on Fig. 12(a), finding the optimum load-pull (LP) impedance at each frequency. The results are presented in Fig. 12(c), where the LP impedance (Z_{LP}) at 210-GHz is $(20 + j22)\,\Omega$. Then, the entire structure of Fig. 10, from the reference plane, to the IC bond pad, the bondwires, and the antenna array, was simulated as a single radiation element. The matching network and array dimensions of the antenna were then both adjusted to obtain $Z_{\text{in}} = Z_{\text{LP}}$ at the reference plane, while maintaining broadside radiation along the z-axis with highest possible efficiency around 210 GHz. The resulting transmitter antenna structure has slightly different patch and feed network elements than those of the antenna test structure of Fig. 6.

Fig. 13 shows the simulated radiation pattern of the transmitter antenna at 214 GHz for the excitation from the reference plane defined in Fig. 10. The simulated antenna gain, radiation efficiency, and system efficiency at 214 GHz are 9.36 dB, 60.4%, and 57.5%, respectively. The simulated gain of the transmitter antenna is 0.65 dB lower than that of the antenna test structure (Fig. 7).

Fig. 14 shows the simulated gain of the transmitter antenna as a function of frequency, with the input port defined as in Fig. 10, and with a reference port impedance ($Z_{\text{ref-TX}}$) equal to the complex conjugate of the load-pull impedance at each frequency, i.e., $Z_{\text{ref-TX}} = Z^{\star}_{\text{LP}}$. For example, at 210 GHz, $Z_{\text{ref-TX}} = (20 - j22)\,\Omega$. In the simulations of Fig. 14 , the transmitter antenna and the InP transmitter IC are matched, in the presence of the bondwires, over 204–223 GHz. The 3-dB bandwidth is about 26 GHz, from 195 GHz to 221 GHz.

C. Receiver Interface

Fig. 15 shows an oblique view of the IC-antenna interface in the receiver module. As with the transmitter IC, signals are carried on the receiver IC with microstrip lines with M4 as the microstrip signal conductor and M1 as the microstrip local ground plane on the IC top surface. TSVs connect the M1 ground plane to the metal on the InP IC back surface. The microstrip signal conductor is connected to the bond pad on M4, and a single wedge-bonded wire-bond connects this pad the antenna substrate signal pad.

Before considering in detail design of the receiver antenna and its impedance-match to the receiver IC, it should be noted that the receiver IC's LNA, when originally reported as a stand-alone amplifier [34], used a very small input pad suitable for wafer probing but not wire-bonding. This design obtained S_{11} better than -8 dB at 210 GHz. When then LNA was subsequently integrated into the 210 GHz receiver [33], the small probe pad was replaced with a larger pad suitable for wire-bonding (Fig. 12(b)). Because at the time of receiver integration the LNA input match was not re-tuned to compensate for the larger parasitics associated with the larger pad, the impedance-matching network on the receiver antenna substrate was designed to compensate not only for the parasitic impedances of the wire-bond, but also for the extra parasitic introduced by the receiver IC bond-pad.

To design this matching network, we first define an input reference plane on the receiver IC at the point labeled as "input" in Figs. 12(b) and 15. With the input reference plane thus defined, the receiver input impedance (Z_{in}) at 190–230 GHz was then simulated at 1-GHz steps and determined at each frequency point. The simulated Z_{in} at 210 GHz is $(35 - j15)\,\Omega$, as shown in Fig. 12(c), where the optimum noise impedance of the receiver ($Z_{\text{opt-noise}}$) is also presented.

We then simulated the entire structure of Fig. 15 as one radiation element, from the reference plane, to the IC bond

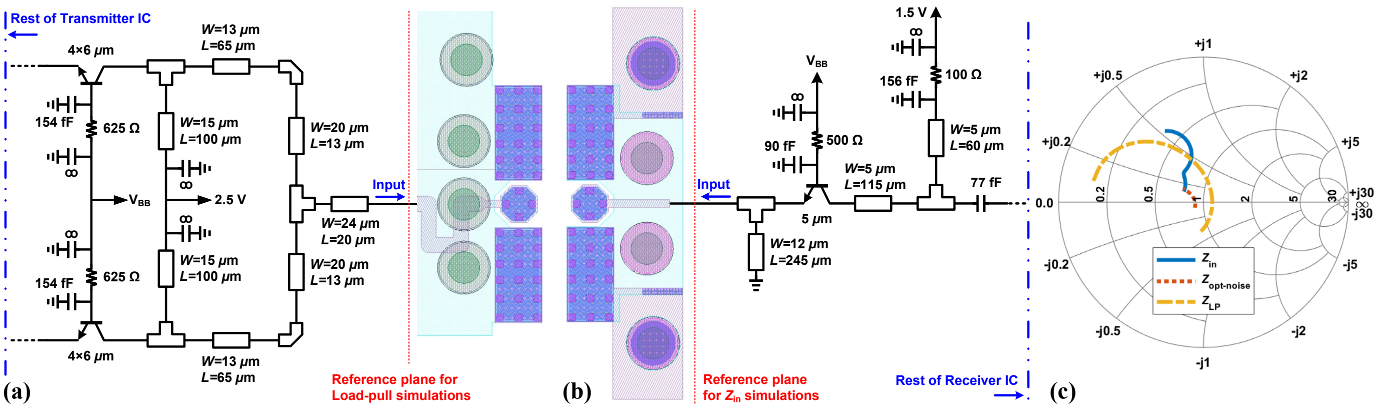

Fig. 12. (a) The last stage of the PA in the InP transmitter IC and (b) the first stage of the LNA in the InP receiver IC. (c) Simulation results, over 190–230 GHz, for the input impedance of the LNA (Z_{in}), optimum noise impedance of the LNA ($Z_{\text{opt-noise}}$), and the load-pull impedance of the PA (Z_{LP}). The reference planes for these simulations are shown by "Input" in (a) and (b), and they are the same as those in Figs. 10 and 15.

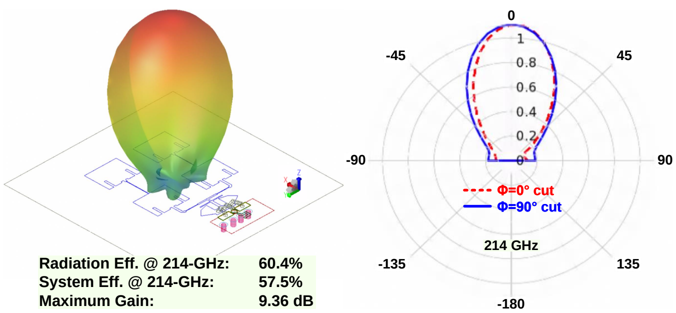

Fig. 13. *E*-field radiation pattern, at 214 GHz, of the transmitter antenna excited from the input port defined in Fig. 10. 0° cut refers to the X-axis (the E-plane), whereas 90° cut refers to the Y-axis (the H-plane).

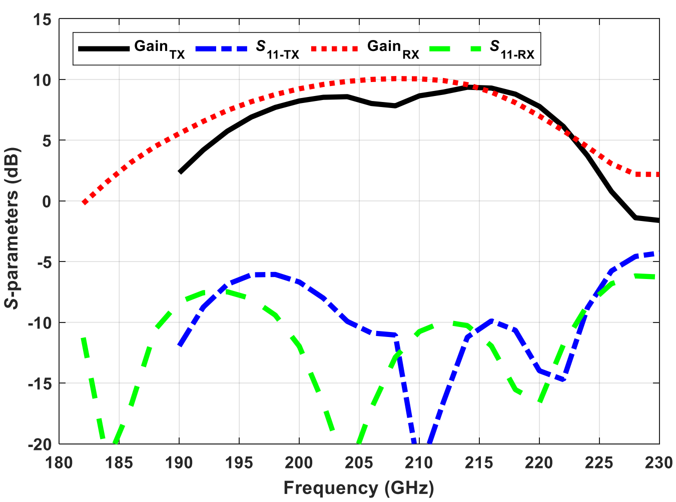

Fig. 14. Simulated gain and S_{11} of the RX and TX antennas excited from the "Input" points in Figs. 10 and 15. The reference impedance for the transmitter simulation is the conjugate complex of the port impedance giving the greatest transmitter P_{sat} at each frequency, i.e., $Z_{\text{ref-TX}} = Z^{\star}_{\text{LP}}$. The reference impedance for the receiver simulation is the input impedance, $Z_{\text{ref-RX}} = Z_{\text{in-RX}}$. Port reference planes are as defined in Figs. 10 and 15.

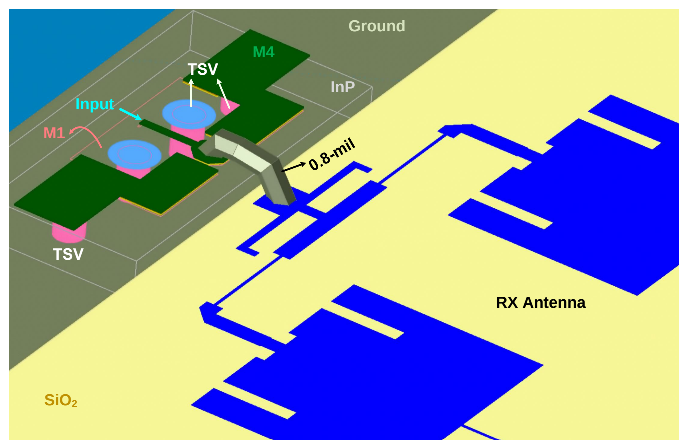

Fig. 15. IC-antenna interface in the receiver module. The point labeled "Input" defines the reference plane for electromagnetic simulations of the IC-antenna interface

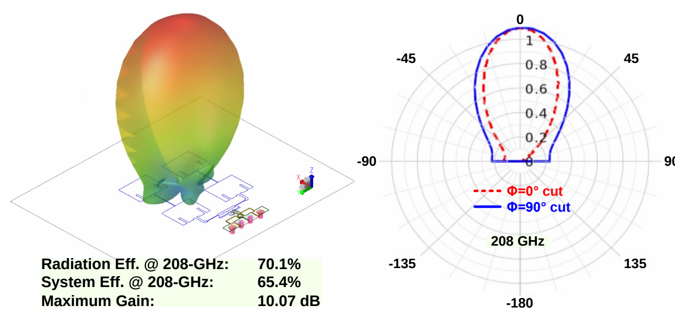

Fig. 16. *E*-field radiation pattern, at 208 GHz, of the receiver antenna excited from the reference plane defined in Fig. 15. 0° cut refers to the X-axis defined in the figure (the E-plane), whereas 90° cut refers to the Y-axis (the H-plane).

pad, the wire-bond, the antenna impedance matching network, and the 2×2 patch antenna array, in Keysight RFpro. The matching network and antenna array were adjusted through extensive simulations to obtain a conjugate matching at the reference plane and maintain the broadside radiation along the z-axis with maximum gain and efficiency around 210 GHz. The resulting receiver antenna array design differs slightly from that of the 2×2 antenna test structure and from the transmitter antenna array.

Fig. 16 shows the simulated E-field radiation pattern of the receiver antenna at 208 GHz, with the excitation at the reference plane defined in Fig. 15. The simulated gain, radiation efficiency, and system efficiency at 208-GHz are 10.07 dB, 70.1%, and 65.4%, respectively. The simulated gain at 218 GHz is almost equal to that of the stand-alone antenna test structure (Fig. 7), which suggests optimal design of the receiver interface. The simulated gain of the receiver antenna versus frequency and the input matching vs. frequency are also depicted in Fig. 14. The excitation point is the reference plane shown in Fig. 15. The 3-dB bandwidth for the antenna gain is 27 GHz (from 193 GHz to 220 GHz), and the S_{11} is better than -10 dB over 198–223 GHz frequency range.

D. Performance Sensitivity to Wire-bonds

As previously explained, the signal lines in the InP ICs and the antennas are connected by a wedge-bonded wire-bond using 20-μm diameter Au wire (Fig. 17(a)). This wire-bond has a considerable impact on the overall performance of the module, and to show this, we re-simulate the performance of the RX antenna, when excited from the "Input" point in Fig. 15, for a wire having lager curvature but same diameter (Fig. 17(b)) as the wire in Fig. 17(a), and a wire having thinner diameter but same shape (Fig. 17(c)) as the one shown in Fig. 17(a). The E-field radiation patterns of the above scenarios are compared in Fig. 17(d), indicating that the radiation pattern at the center frequency is not much affected by the wire-bond characteristics. Fig. 17(e) presents the reflection coefficient at "Input" reference plane in Fig. 15. Since the input matching network of the receive antenna is designed for wire-bond plan of Fig. 17(a), the simulated S_{11} for plans (b) and (c) is worse than the one for plan (a). This also results in an inferior (system) efficiency for plans (b) and (c), as presented in Fig. 17(g). The antenna gain (Fig. 17(f)) is less influenced by the wire-bond shape, leading to only 1 dB less gain for plan (c) compared to the other plans.

We have also studied the effect of wire-bond length on the antenna performance. For this, while keeping the same wire-bond diameter and shape, the center-to-center spacing between the bond pads in the RX antenna and the InP receiver IC was changed by $\pm 20\,\mu$m compared to the default plan of Fig. 17(a), where the IC-antenna pad spacing is $\approx 125\,\mu$m. Similar to the Fig. 17 study, the radiation pattern and antenna gain are not much affected by the wire-bond length variation; however, the S_{11} is impacted by these changes, as shown in Fig. 18. A longer wire-bond degrades S_{11} and shifts it to lower frequencies, whereas a shorter wire shifts the matching response toward higher frequencies. We will get back to this point in Section VI-B.

VI. Measurements

Fig. 19 shows photographs of the overall transmitter modules and close-up images of the ICs, antennas, and wire-bonds. The modules were assembled by Kyocera San Diego. DC power, the LO subharmonic input, and baseband differential (I,Q) signals are connected via wire-bonds to a 203-μm thick PCB using a 127-μm thick I-Tera MT40 dielectric with 35-μm thick copper interconnects having an ENEPIG (electroless nickel electroless palladium immersion gold) surface finish. To provide both mechanical support and heat removal, the IC and the PCB are both mounted, using Ag-filled conductive die-attach epoxy, to a 6.35-mm thick copper carrier electroplated with 5–10 μm nickel (Ni) and 0.5–0.75 μm gold (Au). There are two clearance holes in the metal carrier so that it can be attached to the xyz-positioner to align the module to an external PTFE lens. A PTFE cover protects the InP IC, the antenna substrate, and the wire-bonds.

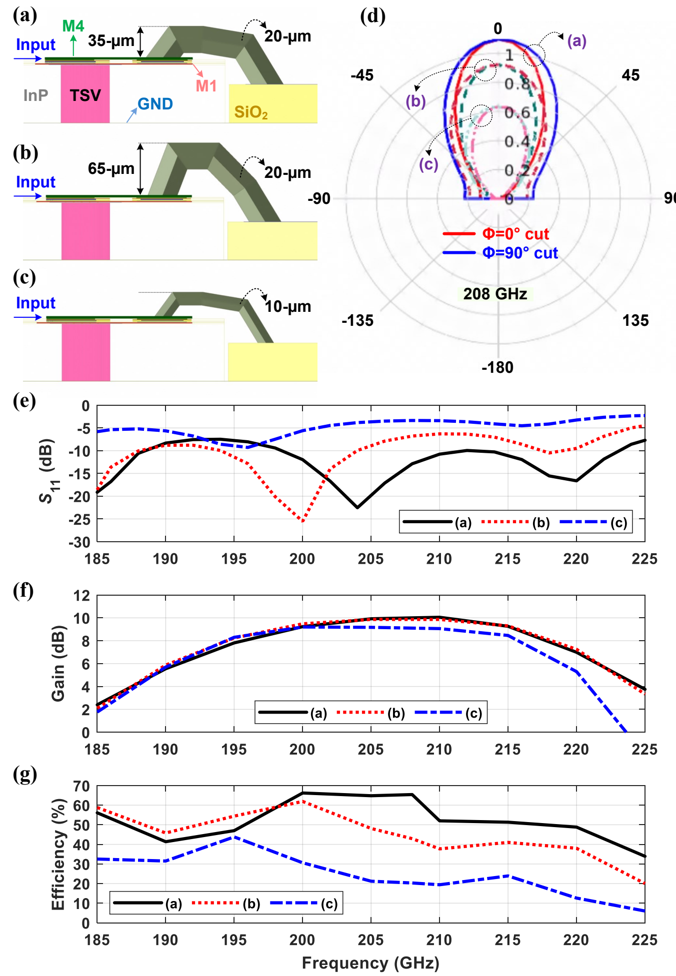

Fig. 17. (a)–(c) IC-antenna interface in the receiver module for default and modified wire-bond shapes. (d) E-field radiation pattern, at 208 GHz, of the receiver antenna excited from the "Input" reference plane in Fig. 15. (e) Input reflection coefficient (at the reference plane), (f) RX antenna gain, and (e) system efficiency of the RX antenna versus frequency for wire-bond plans shown in (a)–(c).

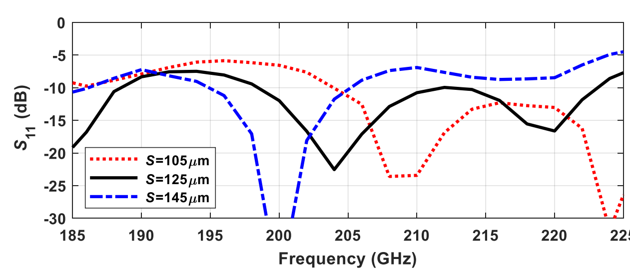

Fig. 18. Input reflection coefficient at the reference plane shown in Fig. 15, when the IC-antenna center-to-center pad spacing (S) is 105 μm, 125 μm (default design), and 145 μm. Wire-bond diameter is 20-μm.

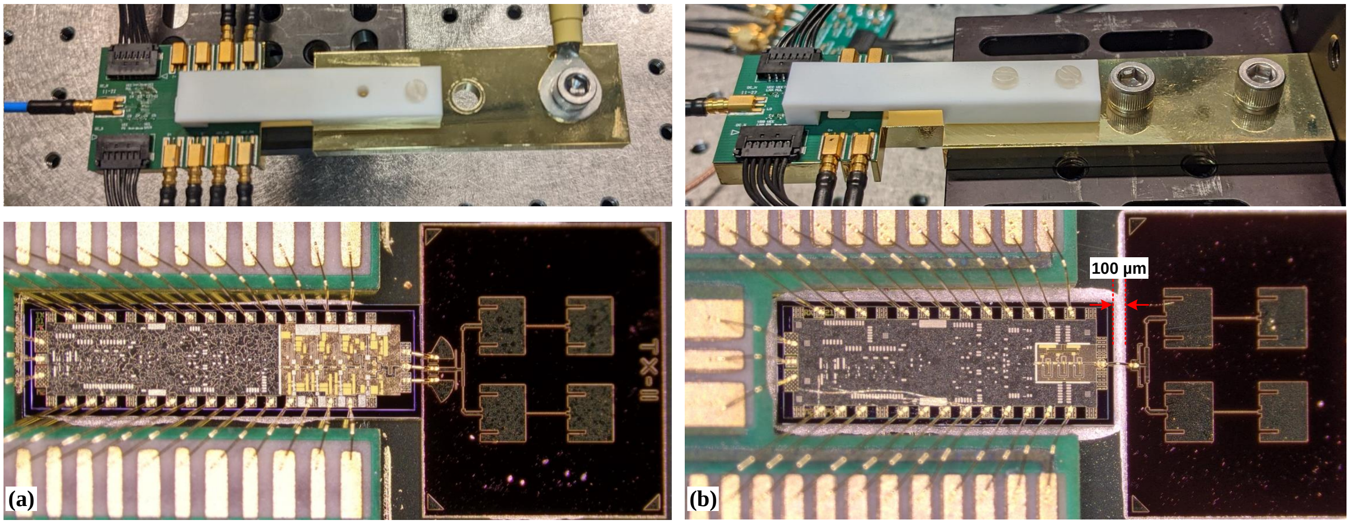

Fig. 19. Photographs of the (a) transmitter and (b) receiver modules, with the top photographs showing the overall modules and bottom photographs showing close-up images of the IC-antenna interfaces.

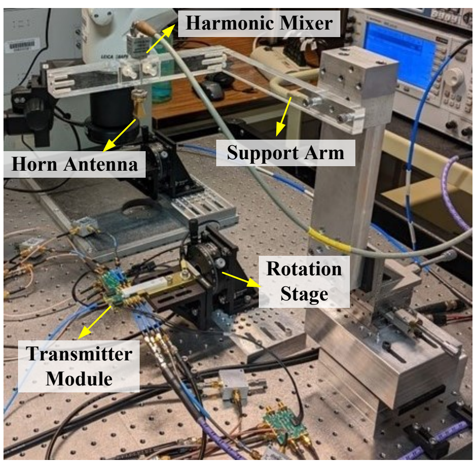

Fig. 20. Transmitter measurement setup for radiation pattern and conversion gain measurements.

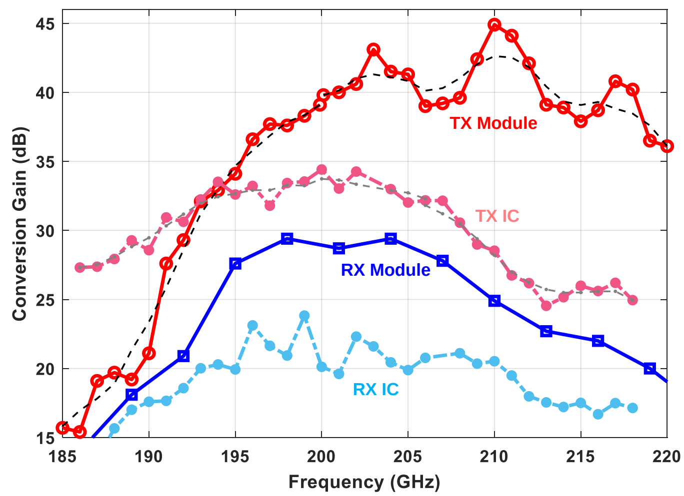

Fig. 21. Measured conversion gain for the transmitter and receiver ICs and modules versus RF frequency. The transmitter module, transmitter IC, receiver module, and receiver IC used local oscillator frequencies of 200, 203, 200, and 207 GHz, respectively.

A. Transmitter Module Results

To test the conversion gain, frequency response, and EIRP of the transmitter module, the baseband (I-channel) input of the module was driven by a sinusoidal input signal, and the power levels of the radiated LO leakage and the up-converted RF upper- and lower-sideband signals were separately measured, at 25.4 cm distance, by a standard-gain G-band horn antenna, down-converted by a G-band harmonic mixer and monitored by a spectrum analyzer (Fig. 20). The power readings of the combined harmonic mixer and spectrum analyzer were calibrated against a power meter (VDI PM5B) using a directional coupler and a 200-GHz source. The power measurements were converted to EIRP using the known propagation distance and the manufacturer's stated horn antenna gain.

Fig. 21 shows the conversion gain of the transmitter module versus the frequency for $f_{\text{LO}} = 200$ GHz. The conversion gain of the transmitter IC (with $f_{\text{LO}} = 203$ GHz) is also shown for comparison. The frequency of peak module gain is approximately 10 GHz greater than that of the transmitter IC; the transmitter module gain-frequency characteristics broadly follow the simulated frequency response of the transmitter antenna (Fig. 14), with a peak of 45 dB at 210 GHz. Neglecting gain-frequency ripple, the transmitter module measured peak gain is approximately 8 dB greater than that of the transmitter IC, consistent with the transmitter antenna simulations; the 10 GHz frequency offset is a result of deliberate center frequency re-tuning during module design.

Fig. 22 shows the measured saturated EIRP of the transmitter module as a function of RF frequency. In this measurement, the LO frequency is kept constant at 200 GHz while the baseband input signal is varied from DC to 20 GHz. This produces both lower and upper modulation sidebands, and the EIRP in the lower and upper modulation sidebands were independently measured. The peak measured EIRP is 24 dBm,

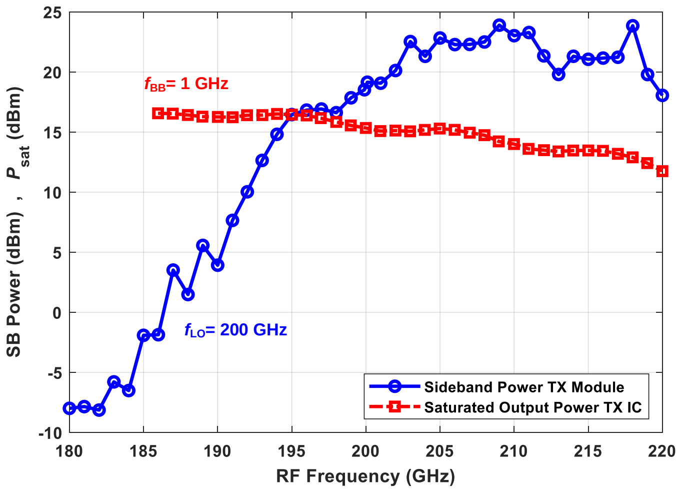

Fig. 22. Measured saturated EIRP of the transmitter module versus RF frequency (given a fixed 200-GHz local oscillator), compared with the saturated output power of the TX transmitter IC (given a fixed 1-GHz baseband input signal).

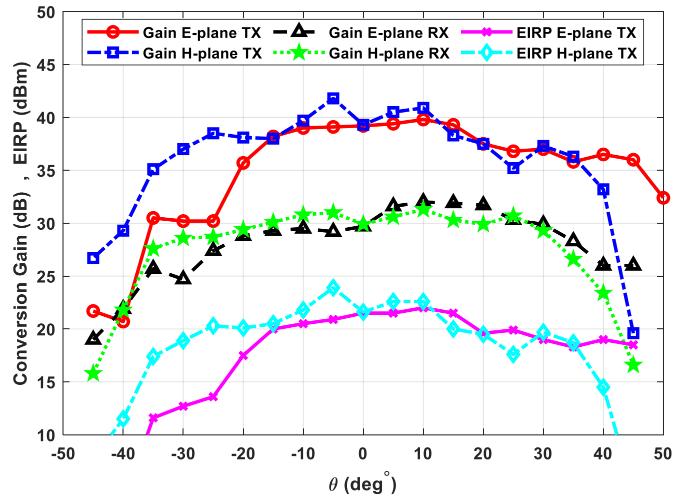

Fig. 24. EIRP of the transmitter module, and conversion gains of the transmitter and receiver modules, as a function of angle in the E-plane and H-plane. For the transmitter measurements, $f_{\mathrm{LO}} = 200\,\mathrm{GHz}$ and $f_{\mathrm{BB}} = 1\,\mathrm{GHz}$. For the receiver measurements, $f_{\mathrm{LO}} = 200\,\mathrm{GHz}$ and $f_{\mathrm{RF}} = 201\,\mathrm{GHz}$.

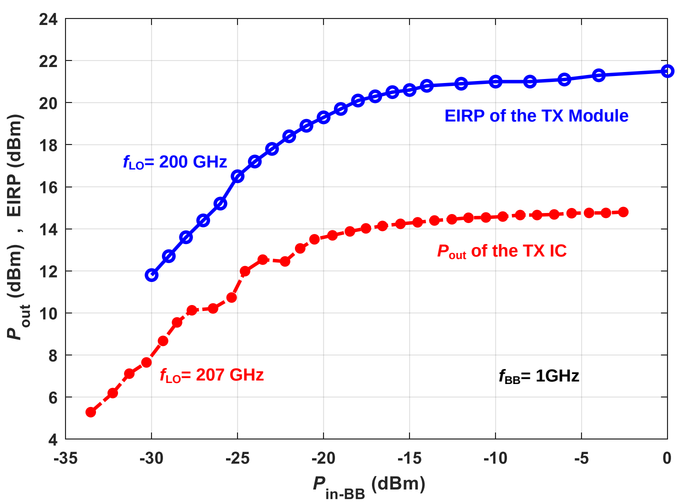

Fig. 23. Measured EIRP of the transmitter module, and measured output power of the transmitter IC, as a function of baseband input power at 1 GHz. The module used a 200-GHz local oscillator, while the IC used a 207-GHz local oscillator.

and it remains greater than 19 dBm over 200-218 GHz. Fig. 23 compares the transmitter module's measured EIRP with the measured output power of the transmitter IC, both as a function of baseband input power. For these measurements, the transmitter module used a 200-GHz LO frequency, while the IC used a f_{LO} of 207 GHz. In both cases, the baseband input frequency is 1 GHz. The input 1-dB compression point of the transmitter module is approximately -21 dBm with a corresponding EIRP of 18.9 dBm, this being 3 dB less than the saturated EIRP.

Fig. 24 depicts the measured gain and EIRP of the transmitter module in the E-plane and H-plane. The measured 3-dB beamwidth of the transmitter module is approximately $\pm 25°$. Therefore, most of power radiated by the antenna can be collected by a lens having a 0.65 numerical aperture, as the latter has a maximum acceptance angle of $\pm 34°$. The measured and simulated beamwidths are similar.

B. Receiver Module Results

In assembly of the receiver module, the antenna substrate was unfortunately placed at a 100-μm separation from the receiver IC, as shown in Fig. 19(b), whereas in the design simulations (Fig. 15), the IC and antenna substrate are in contact. This difference in separation resulted in a longer wire-bond than simulated and degraded the receiver module gain-frequency characteristics, shifting it toward lower frequencies, as predicted in Fig. 18.

To measure the receiver, test signals were generated by a WR-4 2^{nd}-order harmonic mixer with a 100-GHz (subharmonic) LO input and a 0–10 GHz swept-frequency baseband input signal. The mixer output, having upper and lower modulation sidebands and local oscillator feedthrough, was passed through a directional coupler to a standard-gain G-band horn antenna, which illuminated the receiver module from a 12-cm distance. The second port of the directional coupler was connected to a G-band harmonic mixer and spectrum analyzer; this allows the power in the two sidebands to be separately measured. The power readings of the combined harmonic mixer and spectrum analyzer were calibrated against a power meter using a 200-GHz source, and the power measurements were converted to EIRP using the known propagation distance and the manufacturer's stated horn antenna gain.

Fig. 21 compares the measured conversion gain of the receiver module to that of the receiver IC, both as a function of RF frequency. For $f_{\mathrm{LO}} = 200\,\mathrm{GHz}$, the receiver module achieves 29.4 dB peak conversion gain with 3-dB bandwidth of 14 GHz (from 194 to 208 GHz). The measured module bandwidth is markedly lower than that simulated (Fig. 14); this is a consequence of the unintended 100 μm gap between the antenna die and the receiver IC (Fig. 19(b)). Nevertheless, the average gain of the RX module is about 5 to 10 dB higher than the gain of the RX IC.

Fig. 24 shows the measured conversion gain of the receiver module in the E-plane and H-plane. The receiver module has a beamwidth of about $\pm 24^\circ$ for $f_{\text{LO}} = 200\,\text{GHz}$, very similar to the beamwidth of the transmitter when operating at the same frequency, and again very close to that simulated. Consequently, as with the transmitter module, the receiver module can be coupled with high efficiency to a lens having a 0.65 numerical aperture.

C. Link Measurement Results

High-capacity data transmission links have been demonstrated with these modules [36]. The link used 7.1 m transmission range. To avoid receiver overload over this short distance, stacked cadrboard sheets were placed in the beam path to provide 10.4 dB signal attenuation. A further 4.5 dB attenuation was provided by coupling the transmitter 2×2 antenna array, whose 37° acceptance angle was smaller than the antenna 3-dB beamwidth ($\theta_{\text{ant}} \approx 60^\circ$). Without the total attenuation of 14.9 dB, the same link signal-to-noise ratio (SNR) would be obtained at $7.1\,\text{m} \times 10^{14.9/20} = 40\,\text{m}$.

Fig. 25 shows the measured RMS error vector magnitude (EVM), at the receiver, as a function of the transmitter peak EIRP, for QPSK, 16QAM, 32QAM, and 64QAM modulations, with symbol rates varying from 0.5 Gbaud to 9 Gbaud. The red dotted lines indicate the EVM corresponding to 10^{-3} bit error rate for additive white Gaussian noise. Under these EVM limits, 9-Gbaud (18 Gb/s) transmission is demonstrated for QPSK, 8-Gbaud (32 Gb/s) for 16QAM, 5-Gbaud (25 Gb/s) for 32QAM, and 2-Gbaud (16 Gb/s) for 64QAM.

Fig. 26 presents the measured received data constellations, after adaptive equalization, for 9-Gbaud QPSK (15.1% RMS EVM), 8-Gbaud 16QAM (13.5% RMS EVM), and 5-Gbaud 32QAM (10.1% EVM). The performance of mm-wave transceiver modules is summarized in Table I, where the presented modules achieve state-of-the-art results in terms of low-cost integration, conversion gain, and P_{sat}.

VII. Conclusion

We have demonstrated planar 200-GHz transmitter and receiver modules employed for 8-Gbaud 16QAM data transmission (32 Gb/s) over 7.1 m with 13.4% RMS EVM, on a link with 10.4 dB added attenuation. The modules are compact and highly integrated, with only a passive antenna substrate and a single transmitter or receiver IC providing the transmitter and receiver RF-front-end functions. The modules avoid the size and expense of machined waveguide interfaces, instead using a small 2×2 patch antenna array, on a fused silica substrate to provide a radiation pattern with an angular beamwidth compatible with an external lens having a numerical aperture of 0.56. The parameters of the wedge-bonded IC-antenna interface were compensated for by impedance-matching networks on the antenna substrate. The difference between the measured transmitter module gain and the measured transmitter IC gain, and the difference between the the measured receiver module gain and the measured receiver IC gain, are both consistent with the simulated antenna gain, this indicating performance of the assembled modules is close to that predicted by electromagnetic simulations.

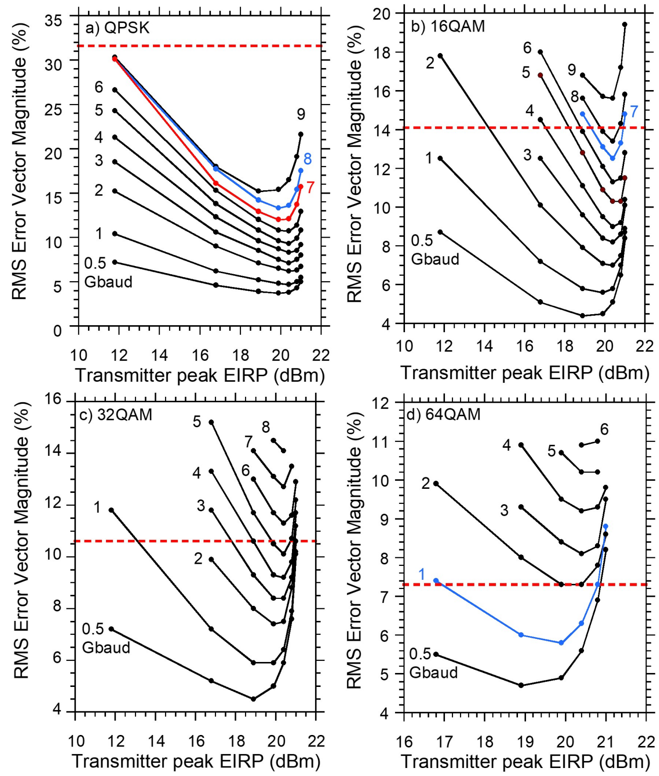

Fig. 25. Link demonstration. Measured RMS error vector magnitude, at the receiver, as a function of the transmitter peak EIRP, for (a) QPSK, (b) 16QAM, (c) 32QAM, and (d) 64QAM modulation, with symbol rates varying from 0.5 to 9 Gbaud [36]. The red dotted lines indicate the EVM corresponding to 10^{-3} bit error rate for additive white Gaussian noise.

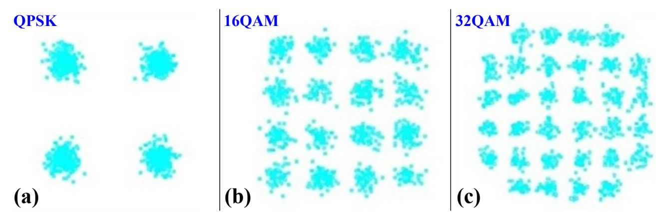

Fig. 26. Received data constellations, after adaptive equalization, for (a) 9-Gbaud QPSK (15.1% RMS EVM), (b) 8-Gbaud 16QAM (13.5% RMS EVM), and (c) 5-Gbaud 32QAM (10.1% EVM) [36].

References

[1] M. J.W. Rodwell, Ali A. Farid, A. S.H. Ahmed, M. Seo, U. Soylu, A. Alizadeh, and N. Hosseinzadeh, "IC and array technologies for 100-300 GHz wireless," in *IEEE Custom Integr. Circuits Conf. (CICC)*, Newport Beach, CA, USA, April 2022, pp. 1-5.

[2] M. J. W. Rodwell, Ali A. Farid, A. S.H. Ahmed, M. Seo, U. Soylu, A. Alizadeh, and N. Hosseinzadeh, "100-300-GHz Wireless: ICs, arrays, and systems," in *IEEE BiCMOS and Compound Semicond. Integr. Circuits and Techn. Symp. (BCICTS)*, Monterey, CA, USA, 05-08 Dec. 2021, pp. 1-4.

[3] G. Xu, S. Abu-Surra, W. Choi, D. Huang, N. Sharma, S. Li, and S. Dong, "THz for 6G communications: vision and challenges," in *IEEE Int. Solid-State Circuits Conf.*, San Francisco, CA, USA, 20-24 Feb. 2022.

[4] R. Nichols, "Measurement and validation of sub-THz radios: What will it take?," in *IEEE Int. Solid-State Circuits Conf.*, San Francisco, CA, USA, 20-24 Feb. 2022.

[5] T. Maiwald, T. Li, G.-R. Hotopan, K. Kolb, K. Disch, J. Potschka, A. Haag, M. Dietz, B. Debaillie, T. Zwick, K. Aufinger, D. Ferling, R. Weigel, and A. Visweswaran, "A review of integrated systems and components for 6G wireless communication in the *D*-Band," *Proc. IEEE*, vol. 111, no. 3, pp. 220-256, March 2023.

TABLE I
COMPARISON WITH RECEIVER AND TRANSMITTER MODULES OPERATING IN 140–300 GHz FREQUENCY RANGE.

†	This Work	RFIC 2020 [15]	MWCL 2019 [31]	IEICE-TE 2015 [21]	JSSC 2020 [24]	IRMMW 2014 [19]
IC Technology	250-nm InP HBT	130-nm SiGe BiCMOS	130-nm SiGe BiCMOS	35-nm InGaAs HEMT	80-nm InP HEMT	35-nm InGaAs HEMT [18]
Antenna Type	2×2 patch array on fused-silica	40-dBi waveguide	Ring	wave-guide horn	off-chip lensed horn	waveguide horn
IC-Antenna Connection	IC-antenna bondwire	radio-on-glass (RoG)	antenna-on-IC	IC-wave-guide bondwire	IC-wave-guide bondwire	IC-wave-guide bondwire
Integration	Integrated TX & RX ICs; antenna-in-package	ICs in RoG package; 34-43 GHz LO	ICs mounted on substrate lens; 16 GHz LO	ICs in WG modules; separate 100-GHz LO WG module	4 WG modules for TX; 4 for RX, 270-GHz LO source	ICs in WG modules; separate 120 GHz LO WG modules
Frequency	200 GHz	145 GHz	230 GHz	300 GHz	300 GHz	240 GHz
Gain TX $\vert$ RX	$40\vert 34$ dB$^{\square}$	$18\vert 65$ dB$^{\triangle}$	$5\vert 7$ dB$^{\square}$	$-3\vert 6$ dB$^{\square}$	$21\vert 3$ dB$^{\square}$	$-4\vert 3.8$ dB$^{\square}$
RX NF	8.5 dB*	8.5 dB*	11 dB*	6.7 dB§	15 dB§	6 dB§
RX $P_{\text{1dB-in}}$	−24 dBm$^{\wp}$	−8 dBm$^{\wp}$	−15 dBm$^{\nabla}$	NA	−17 dBm$^{\nabla}$	NA
TX P_{sat}	15.3 dBm*	13 dBm*	8.5 dBm*	−7 dBm‡	12 dBm‡	−3.6 dBm‡
Area TX $\vert$ RX$^{\diamond}$	$2.17\vert 1.95$ mm^2	NA	NA	$2.44\vert 2.44$ mm^2	$3\vert$NA mm^2	$2.5\vert$NA mm^2 [18]
P_{DC} TX $\vert$ RX	$1.25\vert 0.82$ W$^{\bullet}$	$2.1\vert 1.3$ W	$0.96\vert 0.45$ W$^{\odot}$	NA	$4.5\vert 6.6$ W	NA
Modulation	16QAM	64QAM	16QAM	QPSK	16QAM	8PSK
Rate	32 Gb/s	36 Gb/s	100 Gb/s	50 Gb/s	120 Gb/s	64 Gb/s
Range	7.1 m$^{\wr}$	NA	1 m	1 m	9.8 m	850 m

†Spec values for other works were extracted from their text or otherwise estimated from the plots.
$^{*}P_{\text{sat}}$ of the transmitter IC. *Noise figure of the receiver IC. $^{\ddagger}P_{\text{sat}}$ of the transmitter module. §Noise figure of the receiver module. $^{\diamond}$Chip area.
$^{\triangle}$Conversion gain of ICs. $^{\wp}$For RX IC. $^{\square}$Conversion gain of modules. $^{\nabla}P_{\text{1dB-in}}$ of the RX module. $^{\bullet}P_{\text{DC}}$ for ICs. $^{\odot}P_{\text{DC}}$ for modules.
$^{\wr}$To avoid receiver overload, 14.9 dB of signal attenuation was applied to the signal path between the receiver and transmitter modules.

[6] A. Simsek, S.-K. Kim, M. Abdelghany, A. S.H. Ahmed, A. A. Farid, U. Madhow, and Mark J.W. Rodwell, "A 146.7 GHz transceiver with 5 GBaud data transmission using a low-cost series-fed patch antenna array through wirebonding integration," in *IEEE Radio and Wireless Symp. (RWS).*, San Antonio, TX, USA, 26-29 Jan 2020, pp. 68-71.

[7] S. Dong, N. Sharma, S. Li, M. Chen, X. Zhang, Y. Hu, J. Li, Y. Su, X. Xu, V. Loseu, E. Seok, T. Chi, W. Choi, and G. Xu, "A 140GHz RF beamforming phased-array receiver supporting >20dB IRR with 8GHz channel bandwidth at Low IF in 22nm FDSOI CMOS," in *IEEE RFIC Symp.*, 11-13 June 2023, San Diego, CA.

[8] A. A. Farid, A. S.H. Ahmed, A. Dhananjay, P. Skrimponis, S. Rangan, and M. J. W. Rodwell, "135GHz CMOS/LTCC MIMO receiver array tile modules," in *IEEE BiCMOS and Compound Semicond. Integr. Circuits and Techn. Symp. (BCICTS)*, Monterey, CA, USA, Dec. 2021, pp. 1-4.

[9] K. Eriksson, P. J. Sobis, S. E. Gunnarsson, J. Hanning, and H. Zirath, "InP DHBT amplifier modules operating between 150–300 GHz using membrane technology," *IEEE Trans. on Microw. Theory Techn.*, vol. 63, no. 2, pp. 433-440, Feb. 2015.

[10] A. A. Farid, Ahmed S.H. Ahmed, A. Dhananjay, and M. J. W. Rodwell, "A fully packaged 135-GHz multiuser MIMO transmitter array tile for wireless communications," *IEEE Trans. Microw. Theory Techn.,*, vol. 70, no. 7, pp. 3396-3405, July 2022.

[11] M. Sawaby, N. Dolatsha, B. Grave, C. Chen, and A. Arbabian, "A fully packaged 130-GHz QPSK transmitter with an integrated PRBS generator," *IEEE Solid-State Circuits Lett.*, vol. 1, no. 7, pp. 166-169, July 2018.

[12] M. Ito, T. Okawa, and T. Marumoto, "*D*-band transceiver utilizing 70-nm GaAs-mHEMT technology for FDD system," in *IEEE BiCMOS and Compound Semicond. Integr. Circuits Techn. Symp. (BCICTS)*, Nashville, TN, USA, 03-06 Nov. 2019, pp. 1-4.

[13] M. Wei, N. Baniasadi, E. Chou, H. Beshary, S. Krishnamurthy, E. Alon, and A. Niknejad, "A *D*-Band packaged CMOS integrated transmitter for MU-MIMO applications," in *IEEE Asian Solid-State Circuits Conf. (A-SSCC)*, Taipei, Taiwan, 2022, pp. 6-8.

[14] A. Ahmed, L. Li, M. Jung, and G. M. Rebeiz, "A 140 GHz scalable on-grid 8×8-element transmit-receive phased-array with up/down converters and 64QAM/24 Gbps data rates," in *IEEE RFIC Symp.*, 11-13 June 2023, San Diego, CA.

[15] A. Singh, M. Sayginer, M. J. Holyoak, J. Weiner, J. Kimionis, M. Elkhouly, Y. Baeyens, and S. Shahramian, "A *D*-band radio-on-glass module for spectrally-efficient and low-cost wireless backhaul," in *IEEE Radio Freq. Integr. Circuits Symp. (RFIC)*, Los Angeles, CA, USA, Aug. 2020, pp. 99–102.

[16] M. Oveisi, H. Wang, and P. Heydari, "A study of a millimeter-wave transmitter architecture realizing QAM directly in RF domain," *IEEE Trans. Circuits Syst. I, Reg. Papers*, vol. 70, no. 6, pp. 2243-2256, June 2023.

[17] O. Memioglu, Y. Zhao, and B. Razavi, "A 300-GHz 52-mW CMOS receiver with on-chip LO generation," *IEEE J. Solid-State Circuits*, vol. 58, no. 8, pp. 2141-2156, Aug. 2023.

[18] D. Lopez-Diaz, I. Kallfass, A. Tessmann, A. Leuther, S. Wagner, M. Schlechtweg, and O. Ambacher, "A subharmonic chipset for gigabit communication around 240 GHz," in *IEEE MTT-S Int. Microw. Symp. Digest*, Montreal, QC, Canada, 2012, pp. 1-3.

[19] F. Boes, T. Messinger, J. Antes, D. Meier, A. Tessmann, A. Inam, and I. Kallfass, "Ultra-broadband MMIC-based wireless link at 240 GHz enabled by 64GS/s DAC," in *39th Int. Conf. Infrared, Millimeter, and Terahertz waves (IRMMW-THz)*, Tucson, AZ, USA, 2014, pp. 1-2,.

[20] I. Kallfass, F. Boes, T. Messinger, J. Antes, A. Inam, U. Lewark, A. Tessmann, and R. Henneberger, "64 Gbit/s transmission over 850 m fixed wireless link at 240 GHz carrier frequency," *J. Infrared, Millimeter, and Terahertz Waves*, vol. 36, pp. 221–233, 2015.

[21] I. Kallfass, I. Dan, S. Rey, P. Harati, J. Antes, A. Tessmann, S. Wagner, M. Kuri, R. Weber, H. Massler, A. Leuther, T. Merkle, and T. Kurner, "Towards MMIC-based 300 GHz indoor wireless communication systems," *IEICE Trans. Electron.*, vol. E98-C, no. 12, pp. 1081-1090, Dec. 2015

[22] C. M. Cooke, K. Leong, A. Escorcia, X. B. Mei, T. W. Barton, M. A. Vega, D. L. Wu, and W. R. Deal "A 220 GHz dual channel LNA front-end for a direct detection polarimetric receiver," in *IEEE MTT-S Int. Microw. Symp. (IMS)*, Boston, MA, USA, 02-07 June 2019, pp. 508-511.

[23] Iulia Dan , P. Szriftgiser, E. Peytavit, J.-F. Lampin, M. Zegaoui, M. Zaknoune, G. Ducournau, and I. Kallfass, "A 300-GHz wireless link employing a photonic transmitter and an active electronic receiver with a transmission bandwidth of 54 GHz," *IEEE Trans. on Terahertz Science and Techn.*, vol. 10, no. 3, pp. 271-281, May 2020

[24] H. Hamada, T. Tsutsumi, H. Matsuzaki, T. Fujimura, I. Abdo, A. Shirane, K. Okada, G. Itami, H.-J. Song, H. Sugiyama, and H. Nosaka, "300-GHz-Band 120-Gb/s wireless front-end based on InP-HEMT PAs and mixers," *IEEE J. Solid-State Circuits*, vol. 55, no. 9, pp. 2316-2335, Sept. 2020.

[25] C. Castro, R. Elschner, T. Merkle, C. Schubert, and R. Freund, "Long-range high-speed THz-wireless transmission in the 300 GHz Band," in *3rd Int. Workshop on Mobile Terahertz Systems (IWMTS)*, Essen, Germany, 2020, pp. 1-4,.

[26] D. Wrana, L. John, B. Schoch, S. Wagner, and I. Kallfass, "Short-range wireless transmission using a 295–315 GHz superheterodyne link targeting IEEE-802.15.3d applications," in *51st Europ. Microw. Conf. (EuMC)*, London, United Kingdom, 2022, pp. 205-208.

[27] W. A. Ahmad, M. Kucharski, A. D. Serio, H. J. Ng, C. Waldschmidt, and D. Kissinger, "Planar highly efficient high-gain 165 GHz on-chip antennas for integrated radar sensors," *IEEE Antennas and Wireless Propag. Lett.*, vol. 18, no. 11, pp. 2429-2433, Nov. 2019.

[28] M. d-. Kok, A. B-. Smolders, and U. Johannsen, "A review of design and integration technologies for *D*-band antennas," *IEEE Solid-State Circuits Lett.*, vol. 2, no. 1, pp. 746-758, June 2021.

[29] S. Kang, S. V. Thyagarajan, and A. M. Niknejad, "A 240-GHz fully integrated wideband QPSK transmitter in 65 nm CMOS," *IEEE J. Solid-State Circuits*, vol. 50, no. 10, pp. 2256-2267, Oct. 2015.

[30] T. Pfahler, M. Vossiek, and J. Schür, "Compact and broadband 300 GHz three-element on-chip patch antenna," in *IEEE Radio and Wireless Symp. (RWS)*, Las Vegas, NV, USA, 22-25 Jan. 2023, pp. 139-142.

[31] P. Rodríguez-Vázquez, J. Grzyb, B. Heinemann, and U. R. Pfeiffer, "A 16-QAM 100-Gb/s 1-m wireless link with an EVM of 17% at 230 GHz in a SiGe technology," *IEEE Microw. Wireless Compon. Letters*, vol. 29, no. 4, pp. 297-299, April 2019.

[32] M. Urteaga, Z. Griffith, M. Seo, J. Hacker, and Mark J. W. Rodwell, "InP HBT technologies for THz integrated circuits," *Proc. IEEE*, vol. 59, no. 3, pp. 1051-1067, June 2017.

[33] M. Seo, A. S. H. Ahmed, U. Soylu, A. Farid, Y. Na, and M. J. W. Rodwell, "A 200 GHz InP HBT direct-conversion LO-phase-shifted transmitter/receiver with 15 dBm output power," in *IEEE MTT-S Int. Microw. Symp. (IMS)*, Atlanta, GA, USA, 6-11 June 2021, pp. 378-381.

[34] U. Soylu, A. S. H. Ahmed, M. Seo, A. Farid, and M. J. W. Rodwell, "200-GHz low-noise amplifiers in 250 nm InP HBT technology," in *Europ. Microw. Integr. Circuits Conf. (EuMIC)*, London, United Kingdom, 03-04 April 2022, pp. 129-132.

[35] A. S. H. Ahmed, U. Soylu, M. Seo, M. Urteaga, J. F. Buckwalter, and M. J. W. Rodwell, "A 190-210-GHz power amplifier with 17.7-18.5 dBm output power and 6.9–8.5% PAE," in *IEEE MTT-S Int. Microw. Symp. (IMS)*, Atlanta, GA, USA, 07-25 June 2021, pp. 787-790.

[36] U. Soylu, A. Alizadeh, M. Seo, A. S. H. Ahmed, and M. J. W. Rodwell, "A 202 GHz link using planar transceiver modules," in *IEEE BiCMOS and Compound Semicond. Integr. Circuits and Techn. Symp. (BCICTS)*, 15-18 Oct. 2023, Monterey, California, USA.

[37] K. Carver and J. Mink, "Microstrip antenna technology," *IEEE Trans. Antennas Propag.*, vol. 29, no. 1, pp. 2-24, Jan. 1981.

[38] C. A. Balanis, *Antenna Theory: Analysis and Design,* 4th ed. NJ, USA: Wiley, 2016.

[39] K.-F. Lee, K. M. Luk, and H. W. Lai, *Microstrip Patch Antennas,* 2nd ed. Singapore: World Scientific, 2017.

[40] H. H. Bae, T. H. Jang, H. Y. Kim, and C. S. Park, "Broadband 120 GHz L-probe differential feed dual-polarized patch antenna with soft surface," *IEEE Trans. Antennas Propag.,* vol. 69, no. 10, pp. 6185–6195, Oct. 2021.

[41] M. H. Maktoomi, Z. Wang, H. Wang, S. Saadat, P. Heydari, and H. Aghasi, "A Sub-Terahertz Wideband Stacked-Patch Antenna on a Flexible Printed Circuit for 6G Applications," *IEEE Trans. Antennas Propag.,* vol. 70, no. 11, pp. 10047-10061, Nov. 2022.

[42] M. H. Maktoomi, S. Saadat, O. Momeni, P. Heydari, and H. Aghasi "Broadband Antenna Design for Terahertz Communication Systems," *IEEE Access,* vol. 11, no. 1, pp. 20897-20911, Feb. 2023.
Maktoomi et al., 'Broadband Antenna Design for Terahertz Communication Systems,' IEEE Access, 2023

[43] A. K. Shackelford, K.-F. Lee, and K. M. Luk, "Design of small-size wide-bandwidth microstrip-patch antennas," *IEEE Antennas Propag. Mag.,*, vol. 45, no. 1, pp. 75-83, Feb. 2003.

[44] K.-F. Lee, S. L. S. Yang, A. A. Kishk, and K. M. Luk, "The versatile U-slot patch antenna," *IEEE Antennas Propag. Mag.,*, vol. 52, no. 1, pp. 71-88, Feb. 2010.

[45] S. I. Latif, L. Shafai, and S. K. Sharma, "Bandwidth enhancement and size reduction of microstrip slot antennas," *IEEE Trans. Antennas Propag.,*, vol. 53, no. 3, pp. 7994-1003, March 2005.

[46] C. -C. Wei, C. -T. Fan, T. -H. Chiang, M. -K. Chiu, and S. -P. Ru, "A comparison study of high-frequency performance between ball bonding and ribbon bonding," in *4th Int. Microsystems Packag. Assemb. Circuits Techn. Conf.*, Taipei, Taiwan, 2009, pp. 685-688,